Available online at www.sciencedirect.com
ScienceDirect
International Journal of Non-Linear Mechanics 42 (2007) 596–607
INTERNATIONAL JOURNAL OF NON-LINEAR MECHANICS
www.elsevier.com/locate/nlm

Thermomechanical transitions in doubly-clamped micro-oscillators

Tuhin Sahai[a,*], Rustom B. Bhiladvala[b,c], Alan T. Zehnder[a]

[a]*Department of Theoretical and Applied Mechanics, Cornell University, Ithaca, NY 14853, USA*
[b]*Cornell Center for Materials Research, Cornell University, Ithaca, NY 14853, USA*
[c]*Materials Research Institute and Department of Electrical Engineering, The Pennsylvania State University, University Park, PA 16802, USA*

Received 29 June 2006; received in revised form 27 November 2006; accepted 22 December 2006

Abstract

The small size and low damping of MEMS oscillators give rise to phenomena that are not observed routinely at the macroscopic scale. In this work we document and explain an experimentally observed transition in the response of a doubly clamped micromechanical oscillator with pretension. The transition from softening to hardening is repeatedly observed upon increasing the power of an incident sensing laser beam, a procedure routinely used to improve signal strength during optical detection of resonant motion of microstructures. At intermediate laser power, a novel resonant response that displays characteristics of both softening and hardening in the same sweep, is observed experimentally. Increased laser heating of a structure in tension may be expected to increase softening behavior. Using tools from non-linear dynamics and continuum mechanics, we show that the observed counter-intuitive behavior can be explained by a competition between the opposing responses of linear and non-linear stiffnesses to a change in temperature.

Keywords: Non-linear dynamics; Non-linear vibrations; Bifurcation; Micromechanical resonators; MEMS; Softening; Hardening; Optical detection; Experimental

1. Introduction

The promise of using MEMS oscillators to supply extremely small sensors and time reference devices at low cost and with low power requirements has captured the imagination of industry and academia, leading to a flurry of activity in this field. Recent works have demonstrated potential for a number of exciting applications. For example, Ekinci et al. [1] explore the limit of MEMS oscillators as ultrasensitive mass sensors. Ilic et al. [2] used MEMS oscillators as sensors for the detection of *E. coli*. Blom et al. [3] successfully used MEMS oscillators to measure fluid density and viscosity. MEMS oscillators have also been used as reference oscillators [4] and to demonstrate signal processing [5] functions. Recently, Hoppensteadt and Izhikevich [6] built a theoretical framework for using an array of MEMS oscillators as a mechanical neurocomputer that should, theoretically, be capable of rapid pattern recognition.

Although these systems are large enough that they can be modeled by the continuum hypothesis [7], their small size makes them particularly sensitive to non-linear effects, due to either the inherent non-linear mechanics of the device itself [8,9] and/or to non-linearities in the transduction mechanism and its interaction with the device (see [10,11]). These non-linearities give rise to systems that are rich in dynamics. For example, Turner et al. [12] observed five parametric resonances in a micromechanical system. While non-linearities are often seen as undesirable for several applications based on linear oscillators, Turner et al. [13] recently proposed using the non-linear nature of MEMS oscillators to enhance the sensitivity of mass detection. Whether the non-linearities are desirable are not, it is important to have a complete understanding of the non-linear nature of the device. Once the dynamics are well undersood, this knowledge can be exploited to design for specific performance objectives.

This work reports counter-intuitive non-linear phenomena observed in forced paddle-beam MEMS oscillators with optical detection of motion. We demonstrate the experimental realization of non-linear behavior that can be tuned from softening to hardening by increasing the power of a laser beam focused on

* Corresponding author. Tel.: +1 607 255 8654; fax: +1 607 255 2011.
E-mail address: ts269@cornell.edu (T. Sahai).

0020-7462/$ - see front matter © 2007 Elsevier Ltd. All rights reserved.
doi:10.1016/j.ijnonlinmec.2006.12.009

a silicon nitride MEMS structure with pretension. This transition is counter-intuitive as increased laser heating may be expected to reduce pretension and lead to softening spring behavior. The transition is understood through a thermal–mechanical model in which the linear and the non-linear stiffness contributions are shown to have opposing responses to temperature change.

We start with a description of the experimental setup and observations. We then develop a simple model for the oscillator and estimate its parameters. Continuation algorithms are used to track periodic solutions of the oscillator model and results from numerical continuation are compared to experimental observations.

2. Experimental setup

The MEMS structure shown in Fig. 1(a) is a silicon nitride paddle-beam oscillator. A film stack consisting of a 0.2 μm thick low-stress LPCVD (low pressure chemical vapor deposition) silicon nitride layer over an annealed 1.5 μm thick sacrificial layer of silicon oxide is grown on silicon wafers. Silicon nitride optical constants (n, k), as measured by ellipsometry, are found to be (2.01,0.046). Oscillators with a beam length of 18 μm, beam width of 2.0 μm, paddle size 10 μm square, and a suspended height of 1.5 μm above the silicon floor are fabricated in the silicon nitride layer. Lateral dimensions have a measurement uncertainty within 5%; the uncertainties in film thickness (device and gap thicknesses) are within 4% of the average values; use of the results of finite element method (FEM) simulations does not predict a change in non-linear features for the model within this range. Essentially, the paddle-beam MEMS structure can be viewed as a doubly clamped beam with a flat, square plate at its center. Undercuts at the beam clamping points, typically greater than half the maximum lateral dimension of the largest structure on the chip, are normally obtained when a (usually unwanted) removal of sacrificial oxide support below the clamping points accompanies etching of the oxide required to create the suspended microstructures. Since large undercuts can lead to a reduction in stiffness and coupling to neighboring microstructures, we used an additional step to minimize the undercuts at the beam clamping points. In this step, small holes were first patterned in the nitride film and a timed preetch was used to remove most of the underlying sacrificial oxide, leaving a minimal supporting sliver underneath the intended paddle-beam locations. This reduced the required time for the final releasing etch, as well as the undercut, to about 10% of the normal value; this small undercut was included in FEM simulations.

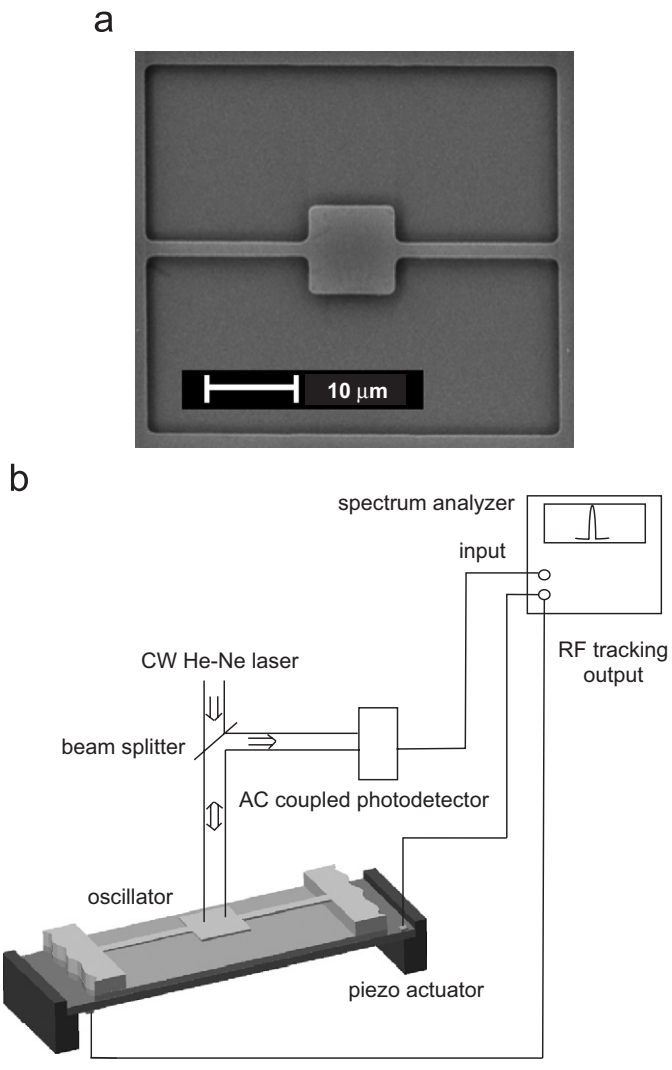

Fig. 1. (a) SEM image of top view of the paddle oscillator. (b) Schematic of the experimental setup.

The oscillator is driven by a piezoelectric disk element from a commercial buzzer with the harmonic driving signal obtained from the tracking generator of a spectrum analyzer. All experiments are performed in a chamber in which a vacuum of 4×10^{-7} torr is maintained. The motion of the paddle is detected by the interferometric modulation of a laser beam (Helium–Neon, 633 nm) focused on the paddle using a microscope objective. The intensity modulation is detected and amplified by an ac-coupled photodetector and converted to spectral information by the spectrum analyzer (see Fig. 1(b)). Other functional details of the experimental setup used here have been described earlier [14,15].

3. Experimental results

Using the setup described in Fig. 1(b) the amplitude of vibration is measured as the driving frequency is swept forward, i.e. from below to above the resonant frequency. Amplitude is also measured as the driving frequency is swept in reverse. Experiments with several micro-oscillators on the same chip, with the same paddle dimensions but with beam lengths varying from 5 to 18 μm revealed a linear torsional mode and nonlinear translational modes, one of which undergoes a softening to hardening transition with increasing laser power. After visually observing this response to a continuous variation of laser power in several device sizes, one size (18 μm beams) is chosen for detailed study. For this device, using a constant forcing amplitude of the piezo drive, the laser power is varied in steps and amplitude response data gathered at each laser power.

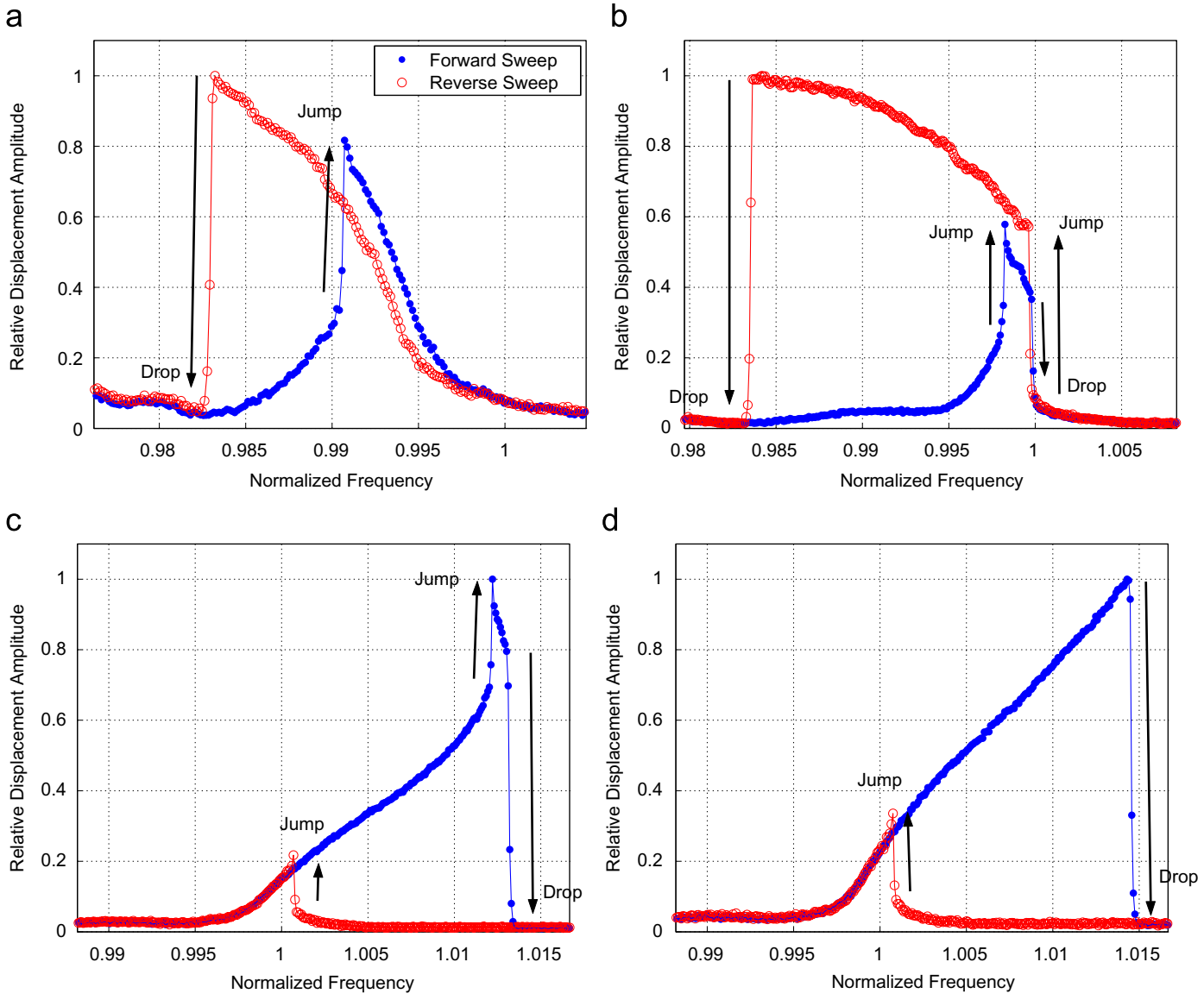

Fig. 2. (Color online) Experimentally obtained (a) softening curve at low laser power, is characterized by a shorter peak and a jump for the forward sweep direction (blue curve) and a taller peak and drop for the reverse sweep (red curve); (d) hardening curve seen at high laser power; (b) and (c) show transitional curves at intermediate laser powers. Curve in (b) has the softening behavior in (a) with an added drop jump feature of (d). The relative laser power for (a):(b):(c):(d) is 5:6:8:9 (one unit 45 μW). All plots are normalized to 0.825 MHz. The amplitudes are normalized by the height of the taller peak in each plot. Each curve is a single sweep in frequency.

The transitional features identified in Figs. 2(b) and (c) were visually confirmed by twice revisiting the same laser power values. The recorded variation in the measurement of power levels is within ±1.4% of the reported value.

The results in Fig. 2 show that as the power of the laser used to detect the motion increases, the response of the first bending mode of oscillation changes from softening, Fig. 2(a), to hardening, Fig. 2(d). Fig. 2(a) shows the jump and drop response expected from a softening oscillator. Figs. 2(b) and (c) show a transition from softening to hardening. The curves in these figures have characteristics of both softening and hardening backbone curves (for a discussion on backbone curves see [16]). The forward and reverse sweeps in frequency each display both a jump and a drop. To the best of the authors' knowledge, no thermo-mechanical systems have been shown to display such transitional behavior. Electrostatically actuated systems, however, have shown softening–hardening transitions [17]. In Fig. 2(d) the system displays pure hardening behavior. The displacement difference between forward and reverse single sweeps seen in Fig. 2(a) is within the bounds of uncertainty for single forward sweeps or reverse sweeps. These sweeps should therefore be interpreted as the same branch, within the limits of experimental error.

The rest of this article is dedicated to understanding and modeling the softening–hardening transition that occurs in optically transduced paddle-beam MEMS oscillators. The

objective of the modeling effort is to capture the essential dynamics that causes the transitions.

4. Theoretical model

Experimentally observed resonance curves (Fig. 2) suggest a stiffness-mediated non-linear response of an oscillator. Estimated effects of photon pressure, Casimir forces and air damping are found to be negligible. Given the size of the oscillator, we model it using a continuum approach. The paddle oscillator has membrane stress contributions from the intrinsic stress in the silicon nitride film, induced thermal strain and large-deflection effects. These membrane stresses result in changing linear and non-linear stiffnesses, thus the Duffing equation is used to model the first translational mode of oscillation of the paddle-beam MEMS structure. The forced Duffing equation can be written as

$$m\ddot{x} + c_d\dot{x} + k_1(x + \beta' x^3) = F\sin(\omega t), \tag{1}$$

where m, c_d and k_1 are the mass, damping and linear stiffness of the spring mass system, β' is the ratio of the cubic stiffness term to the linear stiffness term, F is the forcing amplitude, ω is the forcing frequency, x is the amplitude of deflection of the beam and t is time. Eq. (1) can be rewritten as

$$\ddot{z} + \frac{\dot{z}}{Q} + (z + \beta z^3) = F_s\sin(\omega t), \tag{2}$$

by dividing the entire equation by m, λ (wavelength of the incident laser used to measure deflection) and rescaling time by $\omega_0 = \sqrt{\frac{k_1}{m}}$. In the above equation, $\beta = \beta'\lambda^2$, $F_s = \frac{F}{m\omega_0^2}$, $z = \frac{x}{\lambda}$ and $Q = \frac{m\omega_0}{c_d}$.

Although Eq. (2) captures the mechanical response of the oscillator, it fails to capture the thermal effects of the laser. The incident laser beam is partially absorbed by the MEMS structure; the rest is either reflected or transmitted through the structure. The transmitted light is partially reflected off the silicon substrate and interferes with the light transmitted through the MEMS structure. A Fabry–Perot cavity results from the partial reflections along with the process of interference [10,18]. As the paddle-beam structure oscillates, it is heated or cooled depending on whether the paddle is at a maximum or a minimum of the intensity pattern due to interference.

To model the thermal aspects of the system we use a lumped thermal mass model with Newton's law of cooling. Hence the thermal equation is

$$\dot{T} = -BT + HP_{\text{absorbed}}(z), \tag{3}$$

where T is the temperature of the MEMS structure above ambient, H is the inverse of the lumped thermal mass of the MEMS structure, B is the rate of cooling due to conduction and $P_{\text{absorbed}}(z)$ is the absorbed energy due to the incident laser and is a function of deflection of the structure. Radiation effects are neglected since the most generous estimate shows that cooling due to radiation is less than 3% of the cooling due to conduction. For a more detailed discussion on the thermal modeling see [10]. Time in Eq. (3) is rescaled by ω_0. Thermal membrane stresses affect the bending stiffness, thus Eq. (2) can be written with temperature dependent stiffness terms:

$$\ddot{z} + \frac{\dot{z}}{Q} + f(T)z + g(T)\beta z^3 = F_s\sin(\omega t). \tag{4}$$

The mass, damping, forcing amplitude and frequency are assumed to be independent of T. Eqs. (3) and (4) form a system of equations that model the first mode of vibration of the MEMS structure. We need to estimate the different parameters that are part of the system of equations; they are H, B and $P_{\text{absorbed}}(z)$ in Eq. (3) and Q, $f(T)$, $g(T)$, M and β in Eq. (4).

5. Estimation of parameters

Base units for the analysis are: time: μs, mass: mg, length: μm and temperature: K. The results will, of course, be no different for any other units.

5.1. Thermal parameters and functions

The out-of-plane deflection changes the gap height of the oscillator which in turn influences the interference pattern and the heat absorbed. We model this using the standard formulation of the Fabry–Perot interferometer [18]. A plot of absorption vs. deflection (normalized with respect to λ) is shown in Fig. 3, for 0.2 μm thick silicon nitride with a gap of 1.5 μm,

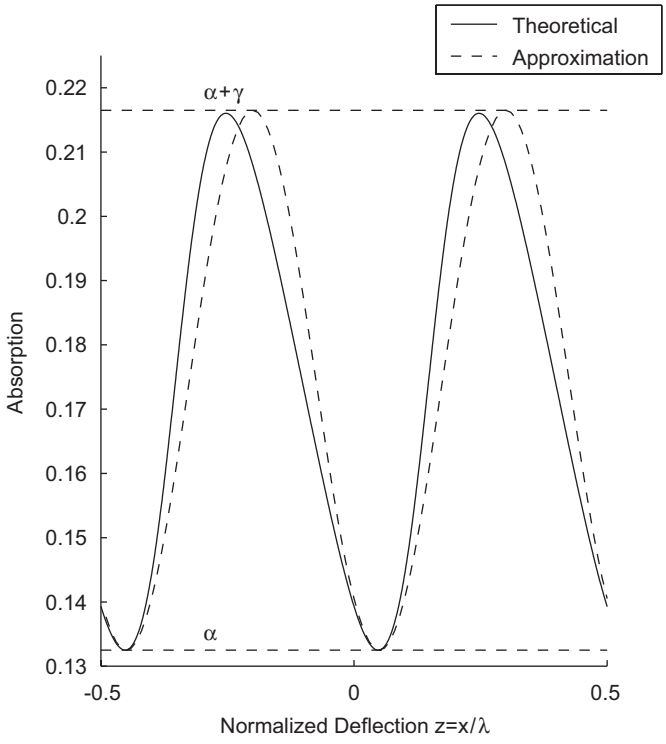

Fig. 3. Plot of absorption vs. normalized deflection of the paddle-beam MEMS structure. Solid line denotes the results obtained from theory [18]. Dotted line denotes the approximation made by $\alpha + \gamma\sin^2(2\pi(z - z_0))$. x is the deflection of paddle oscillator at the location of the laser beam.

Table 1
Material properties of silicon nitride [21,22].

E	300 GPa (calculated)
ρ	2900 kg/m^3
α	1.3×10^{-6}/K
k	3 W/mK
v	0.28

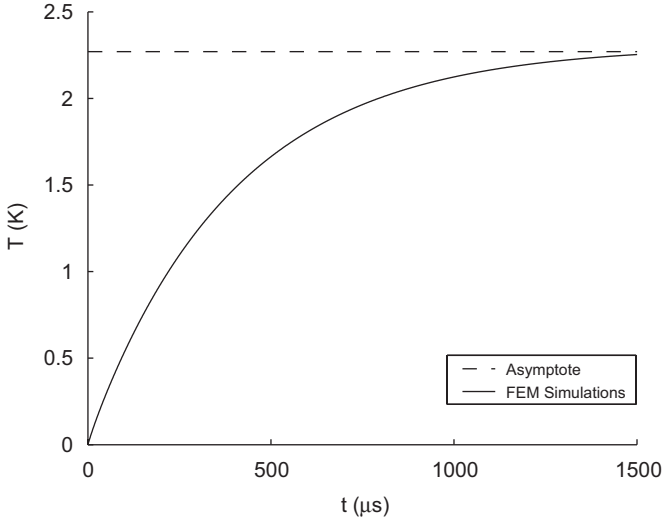

Fig. 4. Plot of temperature vs. time at the center of the paddle for absorbed power of 0.3 μW (obtained from FEM simulations).

and (n, k) values obtained from ellipsometry with no significant change with temperature anticipated [19]. The absorption function P_{absorbed} can be approximated as

$$P_{\text{absorbed}} = P(\alpha + \gamma \sin^2(2\pi(z - z_0))), \tag{5}$$

where P is the applied laser power in μW. From Fig. 3 $\alpha \approx 1.325 \times 10^{-1}$, $\gamma \approx 8.4 \times 10^{-2}$ and $z_0 \approx 5 \times 10^{-2}$. Fig. 3 also gives a measure of how close the approximation, $\alpha + \gamma \sin^2(2\pi(z - z_0))$, is to the theoretical calculation.

To estimate H and B, a thermal finite element model is built and analyzed [20] using the material properties given in Table 1. The boundary condition at the ends of the beam is $T = 0$. The paddle-beam MEMS structure is initialized to $T = 0$. A surface heat flux of 3×10^{-4} μW/μm^2 is applied on the square paddle structure, corresponding to an absorbed power of 0.3 μW. A transient FEM thermal simulation gives the temperature distribution at every step. Since the thermal system is first order, the response of temperature T versus time t will follow the standard first-order response curve (see Fig. 4). This implies that as $t \to \infty$, $T \to \frac{HP}{B}$ (see Eq. (3)). Also, the slope of the response curve at $T = 0$ is $\dot{T} = HP$. Using this information, the values of $H = 2.99 \times 10^{-2}$ K/μW and $B = 4 \times 10^{-3}$ (dimensionless) are obtained after rescaling time with respect to $\omega_0 = 2\pi(0.825)$ rad/μs (experimentally obtained natural frequency). So Eq. (3) now becomes

$$\dot{T} = -BTs + HP(\alpha + \gamma \sin^2(2\pi(z - z_0))), \tag{6}$$

with all the values of the parameters determined.

5.2. Mechanical parameters and functions

The torsional frequency of oscillation of the beam is experimentally found to be independent of the laser power (and hence the tension in the beam). This is to be expected, since the tension does not directly oppose the twisting of the beam, although it does oppose the transverse deflection. Thus, using the measured torsional frequency of oscillation, the value of the shear modulus (G) is computed. Young's modulus E (for silicon nitride) is computed using $E = 2G(1 + v)$ and a handbook value for Poisson's ratio, v, (see Table 1), along with the assumption of isotropy [23]. A discussion on the measurement of the material constants of thin film silicon nitride can be found in [21,22]. The fabrication step leaves the silicon nitride, and hence the beam, in tension. Using the value of E and the measured natural frequency of the bending mode of the beam at low laser powers, the magnitude of pretension is estimated as 50 MPa.

Note that the laser used to measure the motion of the MEMS structure changes its tension. As the moving structure is heated by the laser, the beam expands and the prestress reduces, which in turn changes the stiffness of the structure. Hence, the detection mechanism changes the property of the system that we aspire to measure.

The parameters that need to be estimated in Eq. (4) are Q, F_s, β, $f(T)$, and $g(T)$. The value of the quality factor is estimated to be $Q \approx 1400$ based on experimental resonance curves. We do not have an experimental measure of the magnitude of the forcing, thus a value for F_s which produces a distinct resonance curve with unstable periodic solutions is chosen, resulting in $F_s \approx 5 \times 10^{-5}$.

The cubic stiffness coefficient at $T = 0$, i.e. β, is first estimated by FEM simulation. In the simulation, a uniformly distributed load is applied to the surface of the pretensioned paddle-beam structure and the deflection calculated. The deflection δ at the paddle mid-point is plotted against the total load in Fig. 5. Fitting these points to $k_1(\delta + \beta'\delta^3)$ gives $\beta \approx 0.875$ (after rescaling by λ).

In Eq. (4) the functions $f(T)$ and $g(T)$ (coefficients of linear and cubic stiffness terms) must be determined. As the temperature increases, the pretension in the beam reduces, changing $f(T)$ and $g(T)$. To estimate the two functions, non-linear beam theory is used [24]. Consider the beam in Fig. 6(a). For the sake of simplicity, we assume that the area moment of inertia I, of the beam, remains constant through the length of the beam. Using symmetry arguments, we consider only the right half of the beam (Fig. 6(b)). We start with the Euler–Bernoulli beam equation,

$$M = EI \frac{\mathrm{d}^2 Y}{\mathrm{d}X^2} = SY + M_0 - F(l - X), \tag{7}$$

where

$$S = S_0 + S_i, \tag{8}$$

S is the axial force in the beam, S_0 is the pretension in the structure and S_i is the force induced by deflection, $2l$ is the

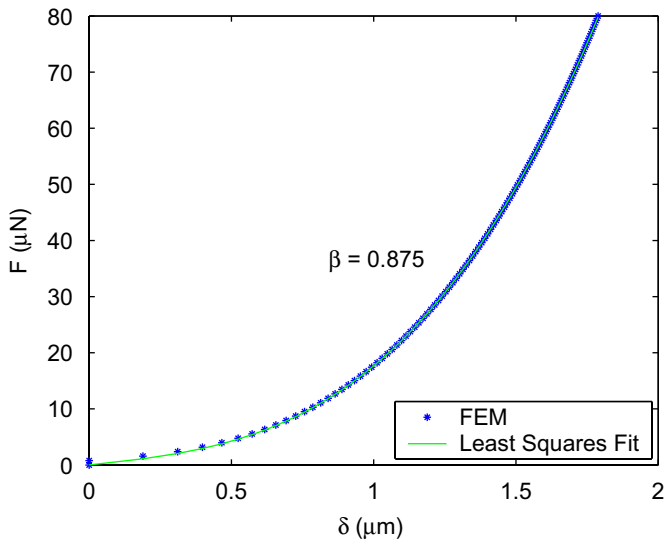

Fig. 5. Plot of force vs. deflection (obtained using FEM simulations).

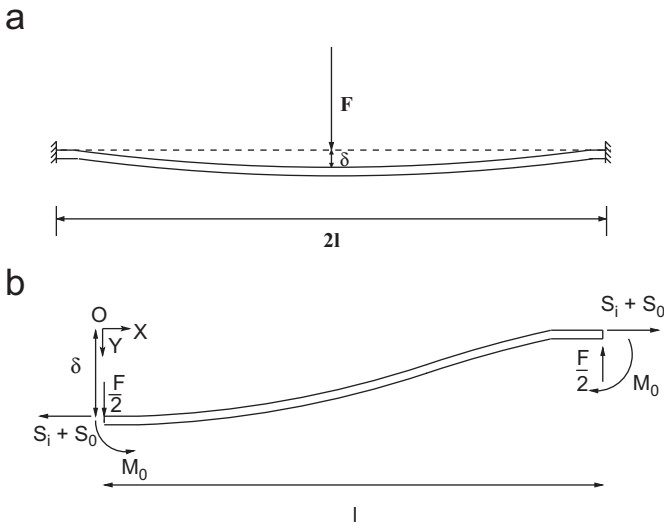

Fig. 6. (a) Doubly clamped beam; (b) FBD of half of the doubly clamped beam (using symmetry).

length of the beam, F is the applied force, Y is the deflection and X is the distance measured from the origin (Fig. 6(b)). The general solution to Eq. (7) is,

$$Y = C_1 \sinh(rX) + C_2 \cosh(rX) + C_3 X + C_4, \tag{9}$$

where

$$r = \sqrt{\frac{S}{EI}}, \tag{10}$$

$C_3 = -\frac{F}{S}$ and $C_4 = \frac{Fl - M_0}{S}$. To determine C_1 and C_2 we use the boundary conditions $(\frac{dY}{dX})_{X=0} = 0$ and $(\frac{dY}{dX})_{X=l} = 0$. This gives us, $C_1 = -\frac{F}{rS}\tanh(rl/2)$ and $C_2 = \frac{F}{rS}$.

To determine M_0 we use $(y)_{X=l} = 0$, resulting in $M_0 = \frac{F}{r}\tanh(rl/2)$. Eq. (9) can now be rewritten as

$$Y = \frac{F}{Sr}[\sinh(rX) - \tanh(rl/2)(1 + \cosh(rX))] + \frac{F}{S}(l - X). \tag{11}$$

At $X = 0$ the deflection becomes $Y_{\max} = \delta$, and

$$\delta = \frac{Fl^3}{4EI}\eta(u), \tag{12}$$

where $\eta(u) = \frac{u - \tanh(u)}{u^3}$ and $u = rl/2$

To determine δ in Eq. (12), we need to determine u, which in turn depends on r. But, from Eq. (10), we know that r is a function of the axial force, S. To determine δ another equation is needed. For this consider the longitudinal elongation of the beam. The length s of the half beam is

$$s = \int_0^l \left[1 + \left(\frac{dY}{dX}\right)^2\right]^{1/2} dX. \tag{13}$$

Assuming that $\frac{dY}{dX}$ is small compared to unity,

$$s \approx \int_0^l \left[1 + \frac{1}{2}\left(\frac{dY}{dX}\right)^2\right] dX = l + \frac{1}{2}\int_0^l \left(\frac{dY}{dX}\right)^2 dX. \tag{14}$$

The change in length of the beam is,

$$\Delta l = s - l = \frac{1}{2}\int_0^l \left(\frac{dY}{dX}\right)^2 dX, \tag{15}$$

thus,

$$S_i = \frac{AE\Delta l}{l} = \frac{AE}{2l}\int_0^l \left(\frac{dY}{dX}\right)^2 dX, \tag{16}$$

where A is the cross-sectional area of the beam (assumed to be constant). Substituting Eq. (11) into Eq. (16) followed by some algebraic manipulation gives

$$S_i(S_i + S_0)^2 = \frac{AEF^2}{2}J(u), \tag{17}$$

where

$$J(u) = \left[\frac{3}{2} - \frac{1}{2}\tanh^2(u) - \frac{3}{2}\frac{\tanh(u)}{u}\right]. \tag{18}$$

But we know (from Eq. (10)) that $S_i = EIr^2 - S_0$, which can be expressed as $\frac{4u^2}{l^2}EI - S_0$. Thus Eq. (17) becomes

$$\left(\frac{4u^2}{l^2}EI - S_0\right)\left(\frac{4u^2}{l^2}EI\right)^2 = \frac{AEF^2}{2}J(u), \tag{19}$$

which can be re-written as

$$F^2 = \frac{2}{AEJ(u)}\left(\frac{4u^2}{l^2}EI - S_0\right)\left(\frac{16u^4}{l^4}E^2I^2\right). \tag{20}$$

The values of F and δ are calculated for a range of u values using Eqs. (20) and (12). This enables us to numerically determine the relationship between force, F, and the deflection, δ,

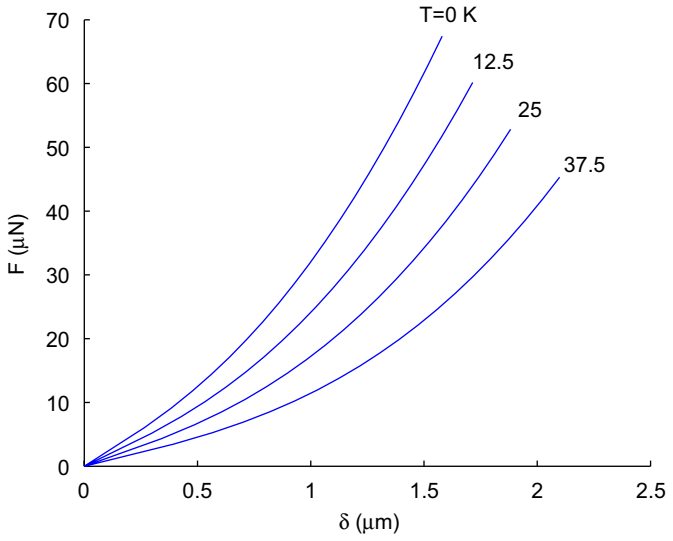

Fig. 7. Plot of force vs. deflection of the beam for different temperatures.

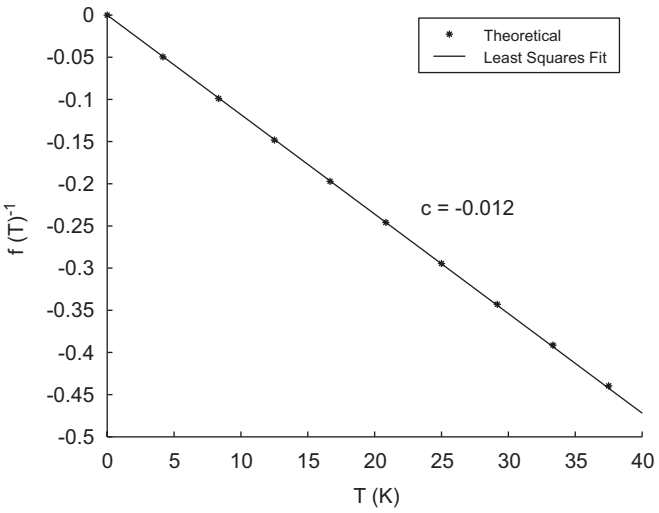

Fig. 8. Plot of the change in linear stiffness vs. temperature.

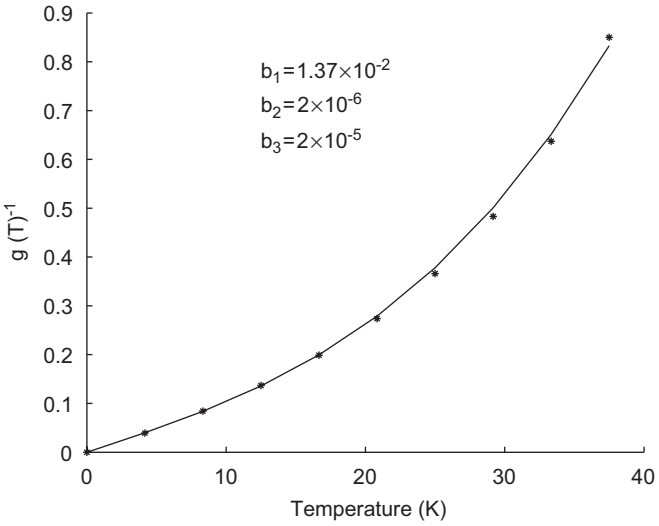

Fig. 9. Plot of the change in cubic stiffness vs. temperature.

at the midpoint of the beam. This procedure is repeated for a range of pretension values S_0. These different pretension values can be related to different temperature values. Using linear thermoelasticity,

$$S_0 = (50\,\text{MPa} - E\alpha T)A, \tag{21}$$

where α is the coefficient of linear expansion (see Table 1). Using the framework constructed in this section we numerically calculate points on the F vs. δ curve for different temperature values (see Fig. 7). A least-squares fit, using $[\delta, \delta^3]$ as the basis functions, is performed for each set of points (corresponding to different temperatures). This gives us the linear and cubic stiffnesses at different temperatures.

It is clear in Fig. 7 that curves corresponding to different temperatures will have different coefficients of linear and cubic stiffnesses. The linear stiffness is given by $f(T)$ and the cubic stiffness is given by $g(T)\beta$. We have already estimated β from FEM simulations. It is also clear that functions $f(T)$ and $g(T)$ should be such that $f(0) = 1$ and $g(0) = 1$. We plot the change in the linear and cubic stiffnesses with temperature in Figs. 8 and 9. The linear stiffness is linear with respect to T, whereas the cubic stiffness is highly non-linear. Thus we model f as $f(T) = 1 + cT$ and g as $g(T) = 1 + b_1T + b_2T^2 + b_3T^3$.

Least-squares fitting approach yields $c = -0.011/\text{K}$, $b_1 = 1.37 \times 10^{-2}1/\text{K}$, $b_2 = 2 \times 10^{-6}1/\text{K}^2$ and $b_3 = 2 \times 10^{-5}1/\text{K}^3$. The functions $f(T) = 1 + cT$ and $g(T) = 1 + b_1T + b_2T^2 + b_3T^3$ are substituted into Eq. (4) to give the system of equations that model the first translational mode of oscillation of the paddle-beam MEMS structure,

$$\ddot{z} + \frac{\dot{z}}{Q} + (1 + cT)z + (1 + b_1T + b_2T^2 + b_3T^3)\beta z^3 = F_s \sin(\omega t), \tag{22}$$

$$\dot{T} = -BT + HP(\alpha + \gamma \sin^2(2\pi(z - z_0))).$$

Note that the linear stiffness term ($\sim z$), with $c < 0$, is thermally softening, while the cubic stiffness term, with β, b_1, b_2, b_3, all > 0, is entirely hardening. It is the competition between these terms that gives rise to the transitions.

A physical explanation for the trends in the stiffnesses of the beam becomes clear once the reason for the non-linearities is understood. Standard beam theory does not take extension of the beam into account. If the same assumption was made in this work, we would fail to model the softening–hardening transitions observed experimentally. As the beam deflects transversely, its length increases, which in turn increases the in-plane stresses. The presence of the in-plane stresses requires that we put a larger incremental force to produce a unit deflection. This is where the cubic term in our model arises from. For high prestress the same deflection of the beam will produce a negligible change in the in-plane stress, making the effect of the non-linearities smaller. This is exactly what the temperature dependence of the linear and cubic terms embodies. The temperature heating due to the laser changes the initial prestress

in the beam, which in turn determines the importance of the non-linearities.

6. Analysis of the model

Using the values of the parameters obtained in the previous section, the numerical analysis of the system described by Eq. (22) is discussed in this section. The primary tool used for constructing the resonance curves of the system is AUTO 2000 [25,26]. AUTO 2000 is a continuation program which is primarily used for bifurcation analyses of algebraic systems and ordinary differential equations (ODEs). It tracks equilibrium and periodic solutions of ODEs with a changing parameter. Our aim here is to numerically track the periodic solutions of the forced system given by Eq. (22) as the forcing frequency ω is varied. Arclength continuation algorithms (such as AUTO 2000) use time t as an internal variable [25,26], hence, the user does not have access to it. So, to compute the periodic solutions of a periodically forced system in AUTO [27], the system of equations given by Eq. (22), is coupled to

$$\dot{v} = v + \omega w - v(v^2 + w^2),$$

$$\dot{w} = -\omega v + w - w(v^2 + w^2). \tag{23}$$

The oscillator given by Eq. (23) has asymptotically stable solutions $v = \sin(\omega t)$ and $w = \cos(\omega t)$. The set of equations that model the first mode of translation of the MEMS oscillator Eq. (22) are coupled to Eq. (23) through v to give the following set of equations:

$$\ddot{z} + \frac{\dot{z}}{Q} + (1 + cT)z + (1 + b_1 T + b_2 T^2 + b_3 T^3)\beta z^3 = F_s v,$$

$$\dot{T} = -BT + HP(\alpha + \gamma \sin^2(2\pi(z - z_0))),$$

$$\dot{v} = v + \omega w - v(v^2 + w^2),$$

$$\dot{w} = -\omega v + w - w(v^2 + w^2). \tag{24}$$

The set of equations given by Eq. (24) are used to obtain the amplitude–frequency response of the system given by Eq. (22). To start continuation, an initial solution to Eq. (24) is needed. However, we do not have a solution to the set of equations except for the case $F_s = 0$ (the equilibrium point can be calculated for this case). To obtain the resonance curves we run a homotopy [28] from $F_s = 0$ to 5×10^{-5} keeping ω fixed (at $\omega = 1.5$ for the reported simulations). What this entails is simply starting the system at equilibrium for $F_s = 0$ and stepping the forcing amplitude at $\omega = 1.5$ until the desired forcing amplitude of $F_s = 5 \times 10^{-5}$ is reached. Then using the solution at $F_s = 5 \times 10^{-5}$ we restart continuation, but this time ω is varied down from $\omega = 1.5$ to 0.0, and in this process the amplitude–frequency curve, at the desired forcing of $F_s = 5 \times 10^{-5}$, is obtained.

Using the process outlined above, the system is studied for a range of laser power values. For $P = 0$ the system is the standard Duffing oscillator. The resonance curve for the system is the classic backbone curve seen in literature [16,29] (see Fig. 10). The curve corresponds to that of a pure hardening spring.As the laser power is increased, the structure heats up and the thermal coefficients of the linear and cubic stiffnesses come into play. For $P = 20\,\mu$W, Fig. 11(a), the system displays a softening response. At $P = 26\,\mu$W the system begins to display characteristics of a softening as well as a hardening system. As the laser power is increased even further to $P = 60\,\mu$W the system displays the softening–hardening jump–drop, as it makes a transition to a hardening system. At $P = 65\,\mu$W the system becomes completely hardening just as in 2(d). The caveat, here, is that there is mismatch between the predicted value of laser power at which the transition occurs and the experimentally observed value. The softening–hardening transition is predicted to occur between $P \approx 22\,\mu$W and $\approx 55\,\mu$W. Experimentally, however, the transition is observed at $P \approx 300\,\mu$W. Constraints from the experimental setup prevented measurement of laser power at the site of the MEMS structure. The measured laser power does not account for attenuation associated with the components in the optical path e.g. lenses and beam splitters; also the laser beam may not be accurately centered on the paddle structure. The coupling between higher modes of oscillation and the first translation mode is also neglected in the model. Given these uncertainties, we do not expect a match betweeen the predicted and measured values of laser power at transition. The structure of the backbone curves obtained numerically (in Fig. 11) is consistent with the experimental results (see Fig. 2). Fig. 12 plots the temperature response. The temperatures are found to be well below the buckling temperature (110 K by Euler buckling).

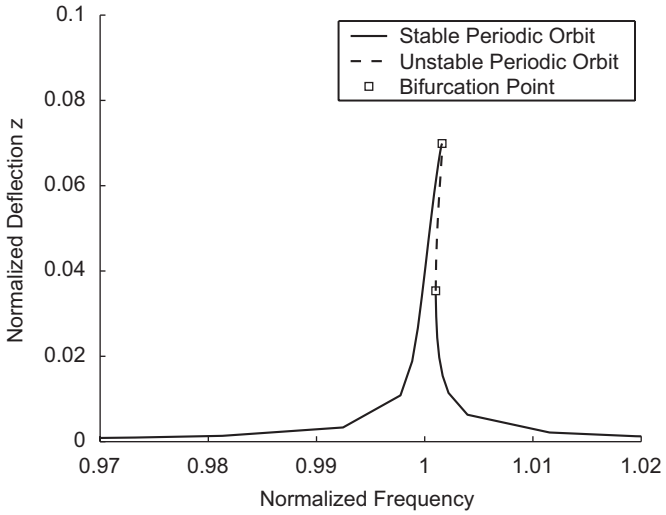

Fig. 10. The classic amplitude–frequency curve for the Duffing Oscillator (obtained at $P = 0$).

Each point on the curves in Figs. 11 and 12 corresponds to the maximum values of z and T achieved in one cycle (for the corresponding value of ω). At any given value of ω multiple periodic solutions may exist, as seen in Figs. 11 and 12. The periodic orbit will depend on its stability and its region of attraction. The points in parameter space where there is a change

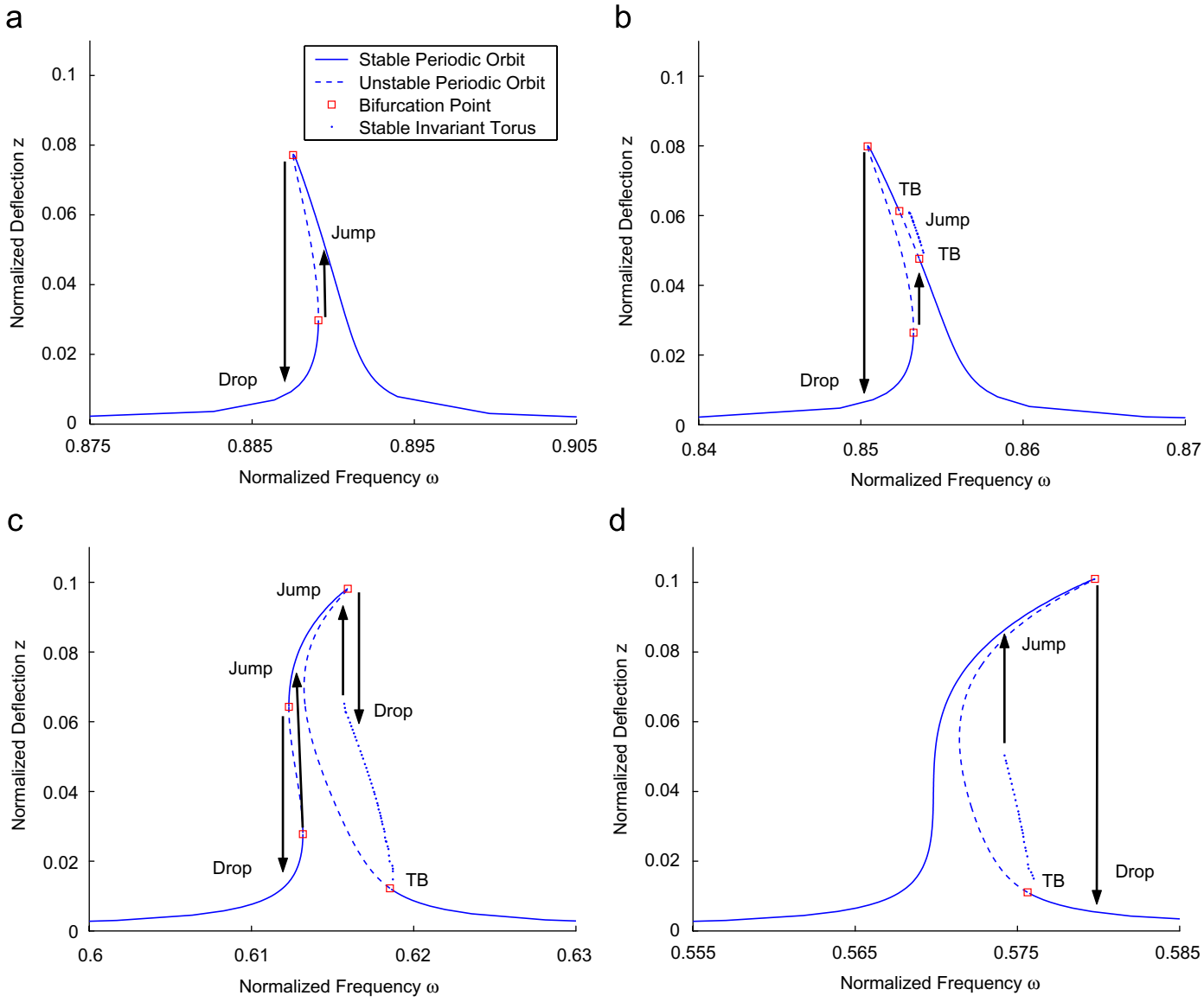

Fig. 11. Maximum deflection vs. frequency at various laser powers. Solid lines denote stable periodic orbits, dotted lines denote unstable periodic orbits, open squares denote bifurcation points and dots denote stable invariant tori: (a) softening at low laser power ($P = 20\,\mu W$); (b) transition from softening ($P = 22\,\mu W$); (c) transition to hardening ($P = 60\,\mu W$); (d) hardening at high laser power ($P = 65\,\mu W$).

in stability or the number of periodic orbits are called bifurcation points. These points have been labeled in Figs. 11 and 12 by an open square. It is important to point out that in Figs. 11 and 12, while sweeping back in frequency the single stable periodic orbit (for high laser powers) loses stability at a torus bifurcation (labeled as TB in the figures). At this bifurcation, the stable periodic orbit is replaced by an unstable periodic orbit and a stable aperiodic oscillation (also known as quasiperiodic oscillations). The quasiperiodic oscillations can be obtained by numerical integration, for example Figs. 13 and 14. We compute these stable tori by successively integrating the system of equations at different parameter values and plot the maximum displacement and temperature along with the continuation results (see Figs. 11 and 12). In this way we can predict the jump and drop locations and hysteresis present in the system. These stable aperiodic orbits will be missed experimentally since the system responds at a combination of frequencies one of which is the driving frequency, and the other is close to the natural frequency of the linear oscillator. The spectrum analyzer detects output in a very narrow band around the driving frequency, thus completely missing the second frequency. These invariant tori lose stability in Figs. 11(c), (d), 12(c) and (d). The reasons behind the loss of stability of these tori will be the subject of future investigation using methods developed in [30]. It is important to point out that although the model does predict the transition from softening to hardening, the exact resonant responses are not achieved. This may be due to unmodeled dynamics, uncertainties in the measured values of optical properties or material properties taken from literature that do not exactly match the material used.

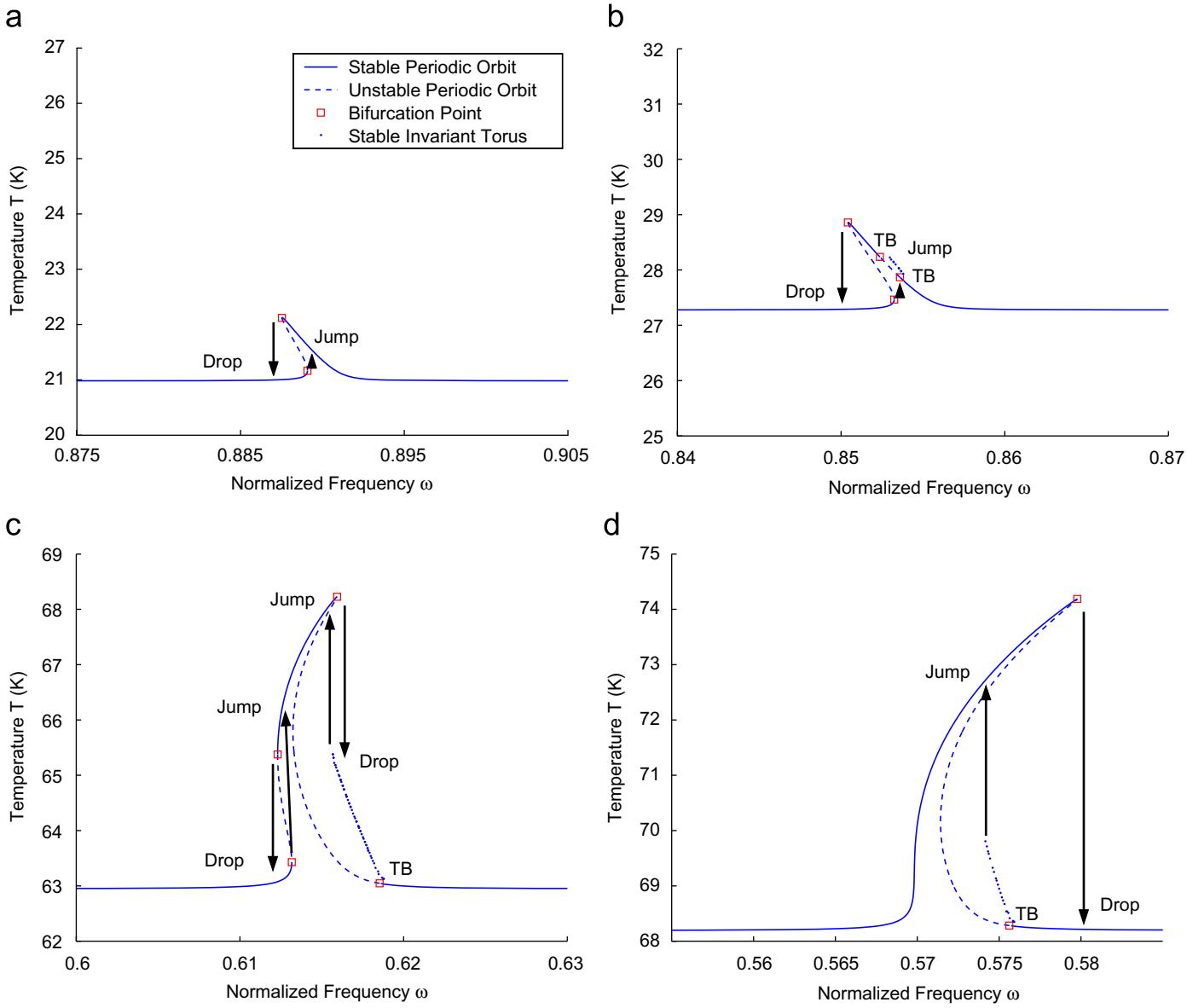

Fig. 12. Maximum temperature vs. frequency at various laser powers. Solid lines denote stable periodic orbits, dotted lines denote unstable periodic orbits, open squares denote bifurcation points and dots denote stable invariant tori: (a) softening at low laser power ($P = 20\,\mu W$); (b) transition from softening ($P = 22\,\mu W$); (c) transition to hardening ($P = 60\,\mu W$); (d) hardening at high laser power ($P = 65\,\mu W$).

7. Conclusions

Although MEMS devices follow the same physical laws governing their macroscopic counterparts, their small size can make them susceptible to effects that are generally negligible in macroscopic objects. This work provides one such example. The paddle-beam oscillators would behave just like large structural beams had it not been for the large changes in tension caused by the laser detection mechanism. The heating due to the laser causes a counter-intuitive transition from softening to hardening behavior of the device. In this work, we ascribe the reason for this transition to the difference in the effect of heating on the linear and cubic stiffnesses of the structure. The linear stiffness makes the system thermally softening, while the cubic stiffness makes the system thermally and mechanically hardening. Large excursions in temperature give rise to large changes in the stiffness terms. We see, in Fig. 12 that a cycle-averaged increase of 60 K is entirely reasonable at high laser powers. A 10 K change in the temperature of the structure will cause about 10% change in pretension, which is ≈ 50 MPa at room temperature. Hence, the temperature (determined by the magnitude of the incident laser power) of the structure dictates whether the thermal softening of the linear stiffness wins over the cubic hardening or not. Since the functional dependence of the linear stiffness term on temperature is different from the cubic term, the temperature range determines if the overall system behavior is softening or hardening. This mechanism is the crux of the softening–hardening transitions. Simulations with

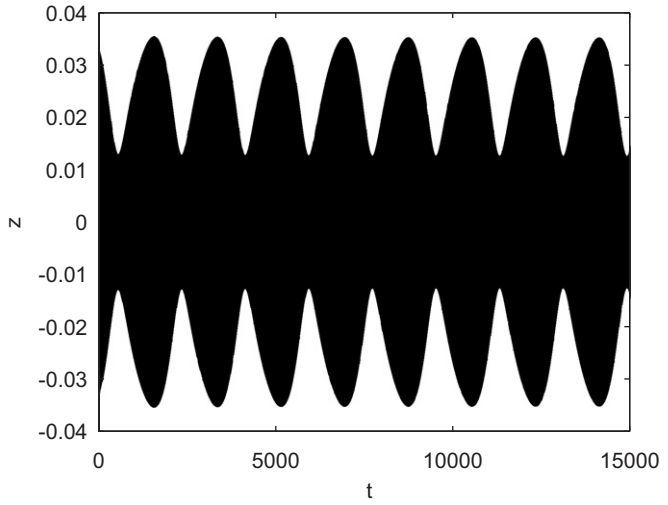

Fig. 13. Quasiperiodic response of the oscillator at $P=65\,\mu W$ and $\omega=0.575$.

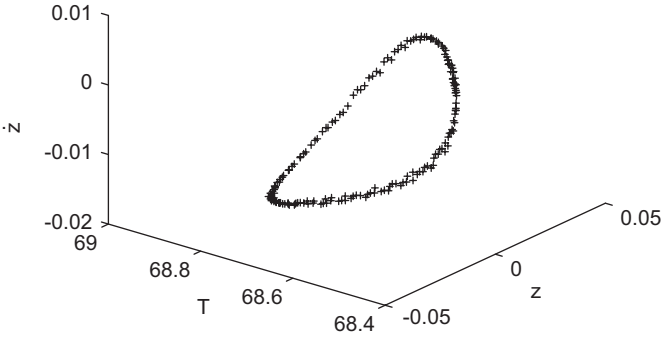

Fig. 14. Poincaré section of quasiperiodic motion at $P=65\,\mu W$ and $\omega=0.575$. Obtained by strobing the system (Eq. (22)) at $t=\frac{2n\pi}{\omega}$ (n is an integer).

the model suggest that the transitions are sensitive to the level of prestress; this provides an example of how non-linear behavior in these small devices may be perturbed or turned off, by identifying and controlling the parameters of greatest sensitivity.

Acknowledgements

The authors thank R.B. Reichenbach for help with the fabrication. This work was supported by the Cornell Center for Materials Research through a National Science Foundation (NSF) grant. All of the fabrication was done at the Cornell Nanoscale Facility (CNF), also supported by the NSF.

References

[1] K.L. Ekinci, X.M.H. Huang, M.L. Roukes, Ultrasensitive nanoelectromechanical mass detection, Appl. Phys. Lett. 84 (22) (2004) 223–256.
[2] B. Ilic, H.G. Craighead, D. Czaplewski, P. Neuzil, C. Campagnolo, C. Batt, Mechanical resonant immunospecific biological detector, Appl. Phys. Lett. 77 (2000) 450–452.
[3] M.T. Blom, E. Chmela, F.H.J. van der Heyden, R.E. Ooterbroek, R. Tijssen, M. Elwenspoek, A. van den Berg, A differential viscosity detector for use in miniturized chemical separation systems, J. Microelectromechanical Syst. 14 (1) (2005) 70–80.
[4] S. Lee, M.U. Demirci, C.T.C. Nguyen, A 10-MHz micromechanical resonator Pierce reference oscillator for communications, in: Digest of Technical Papers, the 11th International Conference on Solid-State Sensors and Actuators (Transducers 01), 2001, pp. 1094–1097.
[5] R.B. Reichenbach, M. Zalalutdinov, K.L. Aubin, R. Rand, B. Houston, J.M. Parpia, H.G. Craighead, 3rd order intermodulation in a micromechanical thermal mixer, J. Microelectromechanical Syst. 14 (6) (2005) 1244–1252.
[6] F.C. Hoppensteadt, E.M. Izhikevich, Synchronization of MEMS resonators and mechanical neurocomputing, IEEE Trans. Circuits Systems 48 (2) (2001) 133–138.
[7] D.E. Segall, S. Ismail-Beigi, T.A. Arias, Elasticity of nanometer-sized objects, Phys. Rev. B 65 (21) (2002) 214109.
[8] X. Zhao, H. Dankowicz, C.K. Reddy, A.H. Nayfeh, Modeling and simulation methodology for impact microactuators, J. Micromechanics Microengineering 14 (2004) 775–784.
[9] S. Rützel, S.I. Lee, A. Raman, Nonlinear dynamics of atomic-force-microscope probes driven in Lennard-Jones potentials, Proc. R. S. London. Ser. A 459 (2036) (2003) 1925–1948.
[10] K. Aubin, M. Zalalutdinov, T. Alan, R. Reichenbach, R. Rand, A. Zehnder, J. Parpia, H. Craighead, Limit cycle oscillations in CW laser driven NEMS, J. Microelectromechanical Syst. 13 (6) (2004) 1018–1026.
[11] M.L. Younis, A.H. Nayfeh, A study of the nonlinear response of a resonant microbeam to an electric actuation, Nonlinear Dyn. 31 (2003) 91–117.
[12] K.L. Turner, S.A. Miller, P.G. Hartwell, N.C. MacDonald, S.H. Strogatz, S.G. Adams, Five parametric resonances in a microelectromechanical system, Nature 396 (1998) 149–152.
[13] K.L. Turner, R. Baskaran, W. Zhang, Using nonlinear dynamics for performance enhancement in resonant micro and nano-scale devices, in: Proceedings of the 42nd IEEE Conference on Decision and Control, 2003, pp. 2650–2651.
[14] D.W. Carr, S. Evoy, L. Sekaric, H.G. Craighead, J.M. Parpia, Measurement of mechanical resonance and losses in nanometer scale silicon wires, Appl. Phys. Lett. 75 (7) (1999) 920–922.
[15] M. Zalalutdinov, J. Parpia, K. Aubin, H. Craighead, T. Alan, A. Zehnder, R. Rand, Hopf bifurcation in a disk-shaped NEMS, in: Proceeding of DETC 2003 ASME Design Engineering Technical Conferences, September 2003.
[16] R. Rand, Lecture Notes on Nonlinear Vibrations, Cornell University, available at ⟨http://www.tam.cornell.edu/randdocs/⟩, 2003.
[17] J.F. Rhoads, S.W. Shaw, K.L. Turner, J. Moehlis, B.E. DeMartini, W. Zhang, Generalized parametric resonance in electrostatically actuated microelectromechanical oscillators, J. Sound Vib. 296 (2006) 797–829.
[18] E. Hecht, Optics, second ed., Addison-Wesley, Reading, MA, 1987.
[19] N.M. Ravindra, S. Abedrabbo, W. Chen, F.M. Tong, A.K. Nanda, A.C. Speranza, Temperature-dependent emissivity of silicon-related materials and structures, IEEE Trans. Semicond. Manuf. 11 (1) (1998) 30–39.
[20] H.D. Hibbitt, B.I. Karlsson, E.P. Sorensen, ABAQUS user manual, Hibbitt, Karlson and Sorensen Inc., 2002.
[21] B.L. Zink, F. Hellman, Specific heat and thermal conductivity of low-stress amorphous Si–N membranes, Solid State Commun. 129 (2004) 199–204.
[22] C.H. Mastrangelo, Y.-C. Tai, R.S. Muller, Thermophysical properties of low-residual stress, silicon-rich, LPCVD silicon nitride films, Sensors Actuators 23 (1990) 856–860.
[23] L.E. Malvern, Introduction to the Mechanics of a Continuous Medium, Prentice-Hall, Englewood Cliffs, NJ, 1969.
[24] R. Frisch-Ray, Flexible Bars, Butterworths, London, 1962.
[25] E.J. Doedel, H.B. Keller, J.P. Kernevez, Numerical analysis and control of bifurcation problems, part I, Int. J. Bifurcation Chaos 1 (3) (1991) 493–520.
[26] E.J. Doedel, H.B. Keller, J.P. Kernevez, Numerical analysis and control of bifurcation problems, part II, Int. J. Bifurcation Chaos 1 (4) (1991) 745–772.

[27] J.C. Alexander, E.J. Doedel, H.G. Othmer, On the resonance structure in a forced excitable system, SIAM J. Appl. Math. 50 (5) (1990) 1373–1418.
[28] J.R. Munkres, Topology, second ed., Prentice-Hall, Englewood Cliffs, NJ, 2000.
[29] J. Guckenheimer, P. Holmes, Nonlinear Oscillations, Dynamical Systems and Bifurcations of Vector Fields, Springer, New York, 1996.
[30] F. Schilder, H.M. Osinga, W. Vogt, Continuation of quasi-periodic invariant tori, SIAM J. Appl. Dynamical Syst. 4 (3) (2005) 459–488.